npj | flexible electronics

Article

Published in partnership with Nanjing Tech University

Article in Press

https://doi.org/10.1038/s41528-026-00652-3

Low-temperature monolithic integration of patterned distributed Bragg reflectors for high-resolution QD-OLED microdisplays

Check for updates

Jin-Wook Shin[1,4], Seung Wan Woo[1,2,4], Hyunsu Cho[1], Sukyung Choi[1], Jun Yong Kim[1], Hyunjun Jang[1,2], Gi Heon Kim[1], In-bok Baek[1], Byoung-Hwa Kwon[1], Nam Sung Cho[1], Chun-Won Byun[1], Hyoc Min Youn[3], Jin Sun Kim[3], Jong Ho Jeong[3], Jung Youn Bae[3], Jonghee Lee[2] ✉ & Chan-mo Kang[1] ✉

With the increasing demand for hyper-realistic displays, significant advancements have been reported in high-resolution quantum dot–organic light-emitting diode (QD-OLED) technology owing to its wide color gamut and improved color purity. However, achieving both high color purity and light extraction remains a critical challenge due to significant blue light leakage in high resolution QD-OLED. Here, we overcome these limitations by demonstrating a damage-free, low-temperature (< 100 °C) monolithic integration of patterned distributed Bragg reflectors (DBRs) directly onto a QD-OLED stack to effectively suppress blue leakage and enhance conversion efficiency. DBRs fabricated from SiN_x and SiO_x using low-temperature (< 100 °C) plasma-enhanced chemical vapor deposition demonstrate high reflectance of 95.9% at 455 nm while effectively suppressing reflectance in the red and green regions. A high-precision, one-step fluorine-based dry etching process achieved a 4 μm pattern size with a near-vertical taper angle of 89°, supporting pixel densities up to 3175 ppi. Compared to the device without DBR, the monolithically integrated architecture exhibits a photon recycling effect, enhancing red and green emission intensities by 19.7% and 10.7%, respectively, while reducing blue leakage by approximately 90%. Furthermore, the integrated device achieved a color gamut of 120.5% relative to the sRGB standard. These findings confirm that monolithically integrated DBRs serve as a robust and scalable solution for next-generation high-resolution QD-OLED displays.

The increased interest in hyper-realistic displays has resulted in extensive research on next-generation displays with high resolution and a wide color gamut[1–3]. To achieve superior color performance, quantum dots (QDs) have emerged as promising materials owing to their excellent optical properties, such as high quantum efficiency, narrow emission spectra, and easy wavelength control[4–6]. These QD down-conversion layers are widely integrated with solid-state blue excitation sources to realize full-color microdisplays. Recently, displays based on III-nitride micro-light-emitting diodes (μLEDs) have developed rapidly, serving as high-efficiency, robust, and ultra-high-brightness optical sources[7,8]. On the other hand, QD-OLED displays, which convert the blue light emitted by the OLED into red or green light via the down-conversion of quantum dots, have been commercialized and represent another key platform for high-performance displays[9–11]. These displays inherit the advantages of conventional OLEDs while providing a wider color gamut owing to the narrow emission spectra of QDs.

However, some technical challenges should be addressed to realize high-resolution QD-OLEDs. Because QD-OLEDs absorb blue light through the QD color conversion layer, any unabsorbed blue light may leak from the device, thereby reducing the conversion efficiency and color purity[12–15]; this issue is exacerbated as the QD layer becomes thinner. The increase in the resolution of QD-OLEDs decreases the size of each pixel, requiring smaller and thinner QD layers. In other words, the thickness of the QD layer must be

[1]Electronics and Telecommunications Research Institute (ETRI), ., Yuseong-gu, Daejeon, Republic of Korea. [2]., Hanbat National University, Yuseong-gu, Daejeon, Republic of Korea. [3]Dongjin Semichem Co., LTD, ., Hwaseong-si, Gyeonggi-do, Republic of Korea. [4]These authors contributed equally: Jin-Wook Shin, Seung Wan Woo. ✉e-mail: jonghee.lee@hanbat.ac.kr; nkcm@etri.re.kr

decreased to achieve high-resolution QD-OLEDs, resulting in a reduced conversion efficiency and color gamut. Therefore, researchers have focused on enhancing the color conversion properties of QDs by adding scattering particles to address the aforementioned problems[16–18]. These scattering particles refract and scatter the incident blue light from OLEDs, increasing the optical path and the amount of light absorbed by QDs, which in turn increases the converted light. Additionally, red and green color filters (CFs) can be applied to the QD layer to prevent blue light leakage[10,12]. CFs selectively transmit specific wavelengths while absorbing others, effectively reducing blue light leakage and increasing the color gamut. However, as CFs do not achieve 100% transmittance, they absorb a part of the red or green light, reducing the conversion efficiency.

Distributed Bragg reflectors (DBRs) have been used to overcome the limitations of conventional CFs[19–22]. DBRs are dichroic mirrors composed of alternating layers of materials with different refractive indices, enabling the adjustment of reflection wavelength regions and reflectance based on the thickness and period of each layer. Applying a DBR that selectively reflects blue wavelengths over the QD layer can not only block leaked blue light but also recycle it by reabsorbing the reflected blue light into the QD layer, thereby enhancing conversion efficiency. Because DBRs reflect blue light, a patterning process should be implemented to remove DBR from the blue pixel region (Fig. 1). However, only a few studies have been reported on DBR patterning owing to the difficulty of multilayer patterning[23]. Crucially, standard dielectric deposition processes often exceed the thermal budget of organic materials, causing irreversible degradation to the underlying OLEDs. Consequently, a monolithic integration strategy operating strictly under low-temperature conditions is not merely advantageous but essential for manufacturing high-yield QD-OLED microdisplays. In thermally evaporated DBR structures based on MoO_3/LiF or WO_3/LiF materials[24,25], high-resolution patterning cannot be achieved because the materials dissolve in water, rendering it impossible to apply photolithography processes. Although SiO_2-based DBR structures can be processed using photolithography, wet etching for DBR patterning is challenging because of the varying etching rates of high- and low-refractive-index materials. Even in the case of dry etching, the low etching rate and selectivity of high-refractive-index dielectrics, such as Nb_2O_5, TiO_2, and Al_2O_3, result in low pattern resolution and poor etch profiles[23,26]. Several studies have investigated the dry etching of DBR using ITO or Cr hard masks[27,28]; however, the additional process of hard mask removal or the high processing temperatures have rendered this approach unsuitable for OLED applications.

In this study, we developed a low-temperature-processed DBR that can be applied to high-resolution QD-OLEDs. The DBR was fabricated via low-temperature plasma-enhanced chemical vapor deposition (PECVD), enabling direct deposition onto the QD layers without causing thermal degradation to the underlying OLED. Furthermore, the DBR consists of SiN_x/SiO_x materials, which facilitate a high-precision, one-step fluorine-based dry etching process for ultra-high-resolution patterning. The optimal thickness and period of the DBR were designed using an optical simulation tool to achieve high reflectance in the blue wavelength region and low reflectance in the red and green wavelength regions. The optical and electrical properties of the fabricated DBR and the QD-OLED with the DBR were evaluated, confirming that the DBR effectively reduces blue light leakage without light loss. Finally, we demonstrated the monolithic integration of the patterned DBR with QD-OLEDs to experimentally verify the photon recycling effect and its impact on enhancing color purity and conversion efficiency. The resulting color gamut performance and patterning resolution were assessed to confirm the feasibility of this integrated approach for next-generation high-resolution QD-OLEDs.

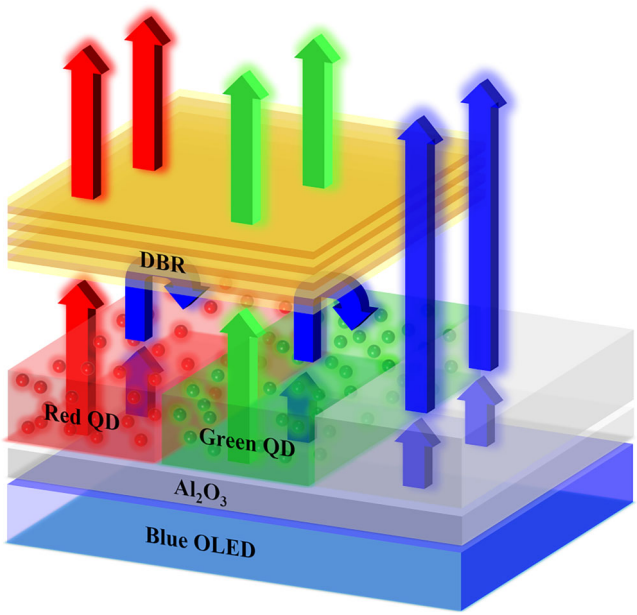


Fig. 1 | Schematic illustration of a patterned distributed Bragg reflector (DBR) integrated into a quantum dot–organic light-emitting diode (QD-OLED) pixel architecture. The QD-OLED consists of a bottom blue OLED backlight layer, an Al_2O_3 encapsulation layer, and patterned red and green quantum dot (QD) sub-pixels alongside a transparent blue sub-pixel region. Upward blue arrows indicate excitation light emitted from the blue OLED layer. The DBR stack is selectively patterned over the red and green QD sub-pixels, while being completely removed from the blue sub-pixel region to permit blue light transmission. Over the red and green sub-pixels, the DBR selectively reflects transmitted blue light downward back into the QD layers (downward blue arrows) for photon recycling and enhanced optical absorption, while allowing converted red and green light (indicated by upward red and green arrows, respectively) to propagate outward.

Results

Structural design of DBR and optical properties

To suppress blue-light leakage in QD-OLEDs, we designed a DBR that exhibits spectrally selective high reflectance in the blue wavelength region. SiN_x and SiO_x were used as the high-and low-refractive-index materials, respectively, and their refractive indices and extinction coefficients are shown in Fig. S1. The reflectance of the DBR (R_{DBR}) is expressed as[29]

$$R_{DBR} = \left[\frac{(n_H)^{2P} - (n_0/n_s)\times(n_L)^{2P}}{(n_H)^{2P} + (n_0/n_s)\times(n_L)^{2P}}\right]^2, \quad (1)$$

where n_H, n_L, n_0, and n_s denote the refractive indices of the high-index layer, low-index layer, incident medium, and substrate, respectively, and P is the number of periods. For a target wavelength of 455 nm, quarter-wave thicknesses ($\lambda/4n$) of 58 nm and 77 nm were selected for SiN_x and SiO_x, respectively.

Transfer-matrix calculations were performed to evaluate the reflectance spectra for the selected SiN_x/SiO_x thicknesses (Fig. S2). As the number of DBR pairs increased from 2 to 10, the reflectance in the blue wavelength region increased markedly, and the stopband edge became progressively steeper. This behavior is attributed to enhanced multiple-beam interference in the periodic multilayer. In particular, the reflectance at 455 nm increased from 14.2 to 97.7%, indicating that increasing the number of periods strengthens the blue reflection and improves spectral selectivity. Despite this improvement, appreciable residual reflection remained at longer wavelengths. For the 10-pair DBR, the reflectance reached 32% (546 nm) and 15.6% (630 nm) at the emission peak wavelengths of green and red QDs, respectively. These long-wavelength ripples arise from constructive interference induced by higher-order resonance modes inherent to the periodic DBR structure[30].

To clarify the physical origin of this residual reflection, an optical-admittance-based analysis was performed. Figure 2a, b depict the conventional DBR structure and the corresponding admittance trajectories at 546 and 630 nm in the complex admittance plane. The reflectivity is governed by the distance between the terminal admittance of the multilayer stack (Y) and

the glass admittance (Y_0), where perfect impedance matching corresponds to zero distance. The admittance trajectory of the conventional DBR terminates far from Y_0, with distances of 1.574 and 0.873 at 546 and 630 nm, respectively, indicating incomplete impedance matching at the DBR/glass interface. To reduce this mismatch, the boundary layers were optimized sequentially. The SiN_x and SiO_x thicknesses at the glass-substrate side were first varied (Fig. S3). This suggests that substrate-side tuning preserves high blue reflectance while modifying the stopband edge and redistributing the long-wavelength spectral characteristics. Based on these results, the glass-side SiN_x and SiO_x thicknesses were selected to 38 nm and 57 nm, respectively.

With this glass-side condition fixed, the SiN_x and SiO_x thicknesses at the air interface were optimized using the admittance-distance maps in Fig. S4. The contour plots of $|Y - Y_0|$ at 546 and 630 nm exhibit distinct minimum regions, indicating that air-side tuning directly governs the terminal admittance condition. To reduce reflectance at both 546 and 630 nm, the air-side SiN_x and SiO_x thicknesses were selected as 10 and 40 nm, respectively. The modified DBR was then designed by combining the optimized asymmetric glass-side and air-side boundary layers, as illustrated in Fig. 2c, d. As a result, the admittance trajectory was substantially reshaped, and the terminal point (Y) shifted closer to Y_0. The corresponding distances decreased to 0.224 and 0.465 at 546 and 630 nm, respectively. This improved impedance matching suppresses the higher-order resonance modes responsible for the long-wavelength ripples.

As shown in Fig. 2e, the calculated reflectance values of the modified DBR are 98.1%, 5.6%, and 6.5% at 455, 546, and 630 nm, respectively, highlighting that the high blue reflectance is preserved while the undesired reflection in the green and red wavelength regions is strongly reduced.

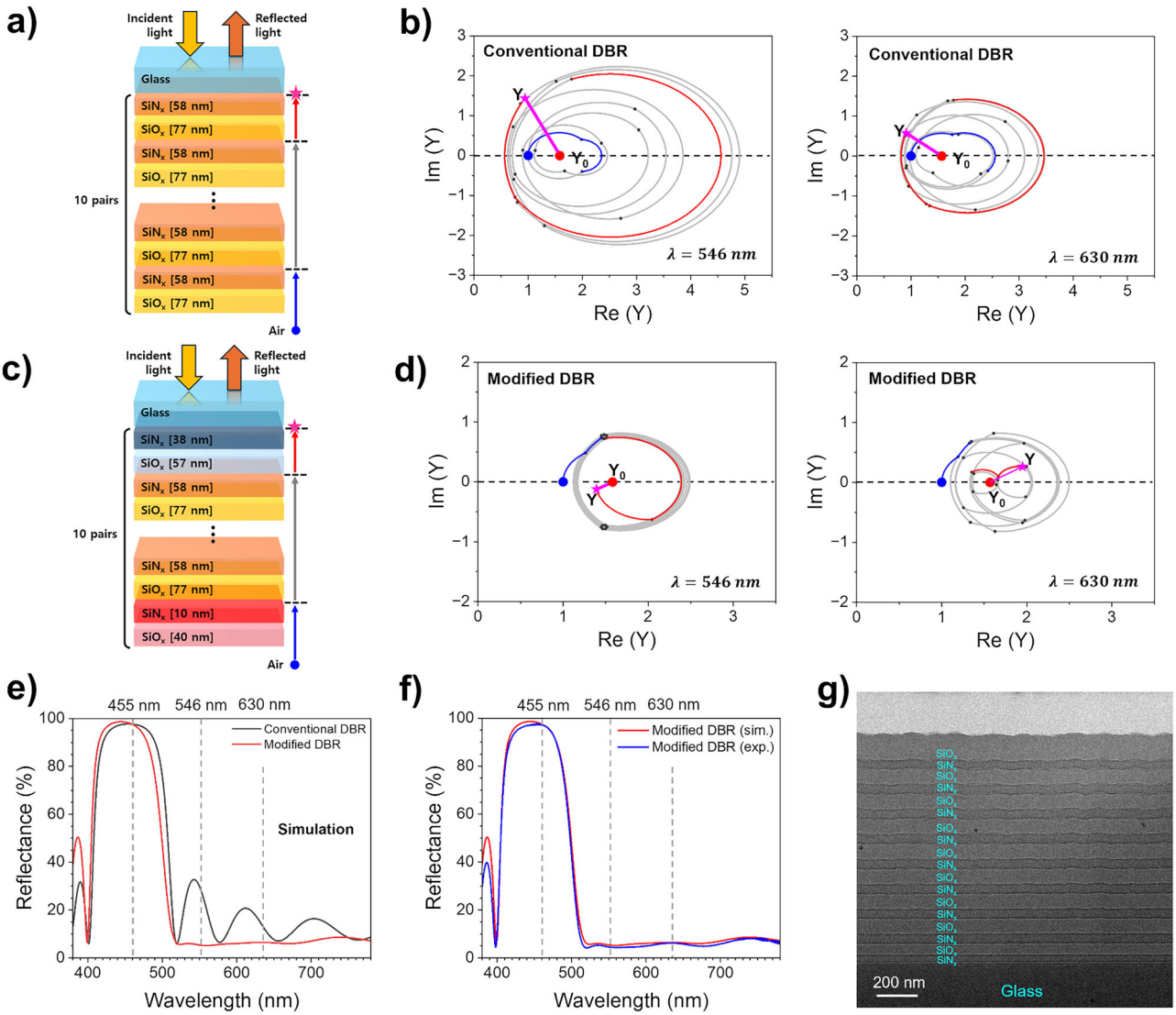


Fig. 2 | Admittance trajectory analysis and optical response of the DBRs. **a** Schematic layer sequence of the conventional 10-pair SiO_x/SiN_x DBR stack on a glass substrate. **b** Optical admittance trajectories of the conventional DBR in the complex admittance plane at wavelengths of 546 and 630 nm, showing terminal admittance points (Y, magenta stars) located at distances of 1.574 and 0.873 from the glass admittance (Y_0, red dots), respectively. **c** Schematic illustration of the modified DBR featuring optimized asymmetric boundary layers at both the glass substrate interface (38 nm SiN_x / 57 nm SiO_x) and air interface (10 nm SiN_x / 40 nm SiO_x). **d** Optical admittance trajectories of the modified DBR, showing that Y shifts closer to Y_0 with reduced distances of 0.224 at 546 nm and 0.465 at 630 nm, effectively suppressing higher-order resonance modes. **e** Simulated reflectance spectra of the conventional DBR (black solid line) and modified DBR (red solid line), demonstrating that high blue reflectance at 455 nm is preserved while unwanted reflections at 546 nm and 630 nm are reduced. Vertical gray dashed lines indicate the target wavelengths. **f** Simulated (red solid line) and measured (blue solid line) reflectance of the modified DBR, exhibiting slightly lower reflectance in the blue region compared to simulation while maintaining comparable levels in the green and red regions. **g** Cross-sectional transmission electron microscopy (TEM) image of the DBR fabricated via the low-temperature-processed plasma-enhanced chemical vapor deposition (PECVD), showing 10 pairs of SiO_x/SiN_x layers on glass along with minor interfacial roughness and thickness variations. Scale bar, 200 nm.

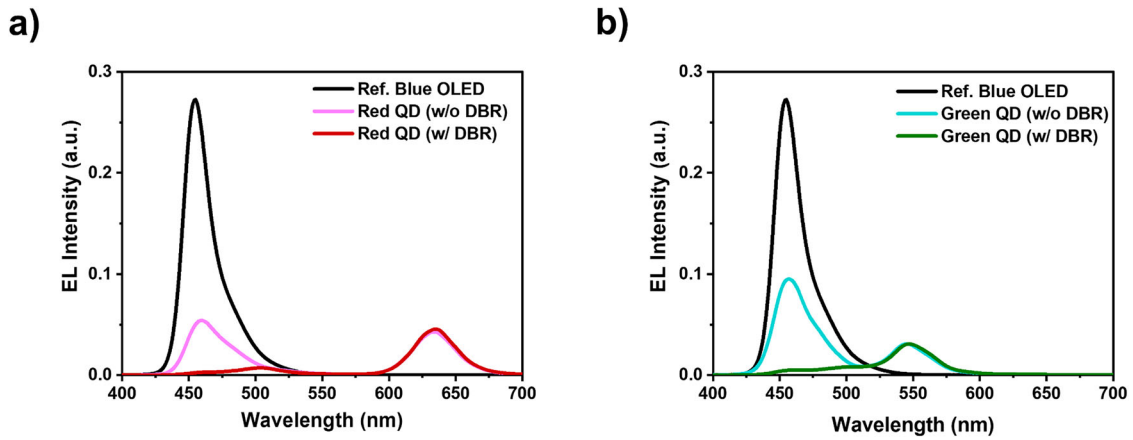


Fig. 3 | Color conversion characteristics of QD-OLED with the DBR. **a** Electroluminescence (EL) spectra of the reference blue OLED (black solid line), red QD layer without DBR (pink solid line), and red QD layer with DBR (red solid line). Without the DBR, unabsorbed blue light leaks through the red QD layer. Upon incorporating the DBR, the residual blue light leakage is suppressed, while the converted red QD emission intensity is maintained. **b** EL spectra of the reference blue OLED (black solid line), green QD layer without DBR (cyan solid line), and green QD layer with DBR (olive green solid line). Similarly, the application of the DBR reduces the transmitted blue light leakage while preserving the green QD emission intensity, indicating that the DBR reduces unabsorbed blue light without degrading the color-conversion performance of both sub-pixels.

Figure 2f compares the simulated and measured reflectance spectra of the modified DBR. The measured reflectance values at 455, 546, and 630 nm are 97.7%, 4.8%, and 6.2%, respectively. Compared with the simulated spectrum, the fabricated DBR exhibits slightly lower reflectance in the blue region while maintaining comparable suppression in the green and red wavelength regions. Furthermore, to verify whether the DBR design optimized on the glass remains effective when directly integrated onto the QD film, additional optical simulations were performed. As illustrated in Fig. S5, the calculated reflectance spectrum at the QD film/modified DBR interface showed a similar overall trend to that obtained for the glass/modified DBR configuration, owing to the comparable refractive indices of the QD film and the glass substrate. This indicates that the optimized DBR can maintain high reflectance in the blue region while effectively suppressing unwanted reflections in the green and red regions, even after integration with the QD film.

Figure 2g presents a cross-sectional transmission electron microscopy (TEM) image of the fabricated DBR, wherein 10 pairs of SiO_x/SiN_x layers are well deposited, yet minor roughness and thickness variations are observed. These morphological imperfections potentially reduced the overall reflectance by decoupling the constructive interference. Notably, the final 10-nm-thick SiN_x layer appears inconspicuous in the cross-section, possibly due to its ultra-thin profile. Importantly, simulation results in Fig. S6 demonstrate that the reflectance spectrum remains substantially unchanged regardless of the presence of this 10-nm SiN_x layer, confirming that its minimal visibility does not compromise the intended optical performance.

Color conversion characteristics of QD with DBR

Figure 3 illustrates the color conversion characteristics of the QD-OLED with DBR. Owing to the application of DBR, the electroluminescent (EL) intensities decreased from 5.01×10^{-2} and 9.42×10^{-2} to 2.29×10^{-3} and 4.58×10^{-3} for red and green QDs at 455 nm, respectively. For a quantitative study, the blue light leakage and output/input (OPIP) rates from the QD color conversion characteristics were calculated as follows[31]:

$$blue\ light\ leakage = I_{BL}/I_{IN}, \quad (2)$$

$$OPIP = I_{QD}/I_{IN}, \quad (3)$$

where I_{BL} denotes the EL intensity of blue light after color conversion, I_{IN} indicates the EL intensity of blue light, and I_{QD} represents the EL intensity of the converted QD light. As indicated in Fig.3, the emission spectra of the blue OLED and red QD are well separated; however, the spectrum of the green QD overlaps with that of the blue OLED. The EL intensity was deconvoluted using a multi-peak Gaussian fitting to separate the green QD spectrum from the blue OLED spectrum (Fig. S7); the detailed parameters are listed in Table S1. In the case of green QD fitting, the peak positions were set to 455 and 472 nm, corresponding to the main and shoulder peaks of the OLED, respectively, and the position at 546 nm represented the emission peak of the green QD. However, in the case of green QD with DBR fitting, achieving an accurate fit was challenging because of the interference caused by the reflectance of the DBR. Therefore, the peak positions at 455 and 546 nm were maintained constant, whereas the remaining parameters were retained as free variables to optimize the peak positions and minimize the fitting error. As indicated in Fig. S7, the EL spectra of the green QD with and without DBR matched well with the fitting function. The deconvolution spectra confirmed that the calculated blue light leakages of the red and green QDs decreased from 26.3% and 41.1% to 4.6% and 5.2%, respectively, indicating that approximately 95% of the blue light was blocked by applying DBR. Moreover, a primary peak of blue light leakage was observed at 504 nm, corresponding to the band edge of DBR. This suggests that blue light leakage can be further reduced by suppressing the long-wavelength vibronic peaks of the blue OLED by employing a strong cavity structure[1,3] or materials with a narrower emission spectrum[32–34]. The OPIP rates were calculated to be 21.4%, 22.5%, 15.5%, and 15.3% for the red QD, red QD with DBR, green QD, and green QD with DBR, respectively. The blue light leakage and OPIP rates for all conditions are summarized in Table 1. The OPIP rates remained similar after applying DBR, indicating that DBR can effectively reduce blue light leakage without compromising QD emissions.

Theoretically, the DBR is expected to enhance the OPIP rate by reflecting the transmitted blue light back into the QD layer, thereby promoting photon recycling. However, the observed OPIP rates remained similar even after applying the DBR. This is likely owing to the current measurement configuration, in which the DBR glass and the QD-OLED

Table 1 | Blue light leakage and OPIP rates of the QD-OLED with DBR

	Red QD		Green QD	
	w/o DBR	w/ DBR	w/o DBR	w/ DBR
Blue light leakage (%)	26.3	4.6	41.1	5.2
OPIP rate (%)	21.4	22.5	15.5	15.3

were fabricated independently and characterized in a stacked assembly. This assembly inevitably introduces an interfacial air gap between the DBR and the QD layer which could potentially limit efficient photon re-absorption and subsequent recycling. In this regard, adopting an integrated structure that eliminates the air gap would be beneficial in clarifying the contribution of photon recycling to the overall device performance.

For practical applications, evaluating the operational durability of the QD conversion layer is an important consideration. In our proposed structure, the QD layer is passivated by the overlying inorganic DBR stack, which helps shield the layer from environmental moisture and oxygen. Under such passivated conditions, the overall durability of the color-conversion layer is closely related to its intrinsic photostability against continuous blue light excitation. To assess this factor, the photostability of encapsulated red and green QD thin films was evaluated under continuous 450 nm blue light irradiation (Fig. S8). The red and green QD films maintained 91.8% and 88.9% of their initial PL peak intensity after 1000 h, respectively. These results indicate that combining inorganic DBR passivation with photostable QD formulations contributes favorably to the operational durability of the QD color-conversion architecture.

Fine patterning of DBR for high-resolution QD-OLED displays

A high-precision fine-patterning process was developed for the DBR to verify the feasibility of implementing high-resolution QD-OLED displays. Since the DBR is designed to reflect blue light, its selective removal from the designated blue pixel regions is essential to ensure high extraction efficiency for the primary blue emission. The primary technical challenge in patterning multi-layered dielectric stacks lies in maintaining a consistent etch rate and anisotropy across chemically distinct layers. In particular, TiO_2, commonly utilized as the high-refractive-index material in conventional DBRs, is notoriously difficult to dry etch due to the low volatility of its reaction byproducts (e.g., TiF_x or $TiCl_x$). This often necessitates high-power plasma conditions or complex chlorine-based chemistries (Cl_2/BCl_3), which can lead to mask erosion and a degraded taper angle[35,36].

The SiN_x/SiO_x material system provides a significant tactical advantage in fabrication over conventional SiO_2/TiO_2-based DBRs. The silicon-based DBR architecture enables a streamlined, single-step dry etching process using a unified fluorine-based gas chemistry. Unlike TiO_2-based systems that often require chlorine-based chemistries, this fluorine-based approach allowed for the rapid patterning of the entire 20-layer stack (10 pairs) in a single 380-second session without periodic gas switching. The relatively high Ar flow rate facilitated directional ion bombardment, which, combined with the chemical etching of CF_4, maintained high anisotropy even at a moderate pressure of 70 mTorr.

Figure 4a depicts a cross-sectional image of the patterned DBR, which exhibits a nearly vertical etch profile with a smooth sidewall morphology. Notably, the taper angle reached approximately 89°, significantly higher than values typically reported for dry-etched dielectric stacks using photoresist mask[23,26]. This highly anisotropic profile demonstrates the excellent directional control of the developed process, which is essential for maximizing the effective aperture ratio and minimizing unintended lateral light leakage at the pixel boundaries. As shown in Fig. 4b, a pattern size of approximately 4 μm was achieved, which corresponds to a pixel density of 3175 pixels per inch (ppi). These results underscore the potential of the developed DBR architecture for integration into ultra-high-resolution microdisplays, providing a robust and scalable solution for augmented and virtual reality (AR/VR) applications.

Monolithically integrated QD-OLEDs with patterned DBR

To experimentally verify the photon recycling effect and address the limitations of the stacked configuration, a monolithically integrated QD-OLED architecture was realized as illustrated in Fig. 5a. The device was fabricated on a silicon substrate integrated with pixel electrodes and address lines, upon which a top-emission blue OLED was deposited as the primary light source. A thin-film encapsulation (TFE) layer was applied over the OLED stack for protection, followed by the patterning of a pixel defining layer (PDL) and QD color conversion layers via photolithography. To prevent thermal degradation of the underlying OLED, both the PDL and QD processes were limited to temperatures below 100 °C. The PDL, patterned from a transparent photoresist, serves a dual structural role: it acts as a protective barrier over the blue sub-pixels and simultaneously forms recessed wells to define the red and green QD deposition regions. Following the QD/PDL formation, an Al_2O_3 buffer layer was deposited to provide QD protection and serve as an etch-stop layer for the subsequent DBR patterning. Finally, the multi-layered DBR was monolithically integrated and selectively patterned to reside exclusively over the green and red QD pixels. The development of this low-temperature PECVD DBR process enabled the monolithic integration of the entire architecture, providing a robust platform to suppress blue light leakage and enhance the photon recycling effect, which is particularly beneficial for high-resolution displays where the QD thickness is inherently limited.

The practical implementation of the proposed monolithic architecture was successfully demonstrated on a 6-inch wafer, as shown in Fig. 5b. The wafer clearly distinguishes between regions with and without the DBR. The DBR-integrated region on the left exhibits a distinctive bluish tint, which is attributed to the selective reflection of blue light by the DBR, whereas the right portion displays the area without the DBR. A magnified image in Fig. 5b shows a single 20 mm × 20 mm device chip extracted from the wafer. Each chip contains 16 distinct 2 mm × 2 mm patterned QD arrays, confirming that the high-resolution patterning process is consistent across multiple devices. Figure 5c shows optical microscopy (OM) image of the pixel arrays, which verify the successful formation of the 200-ppi pixel layout with a sub-pixel size of 60 μm. The OM images confirm that the DBR is precisely aligned over the red and green pixels while being entirely removed from the blue pixel regions to allow for blue emission.

Figure 5d presents the cross-sectional SEM image of the monolithic integration of the QD-OLED with a patterned DBR. The QD layer and the transparent PDL exhibited well-controlled thicknesses of approximately 7 μm and 6 μm, respectively. The cross-sectional view reveals that the DBR stack is selectively patterned on top of the QD sub-pixel, confined within the boundaries of the PDL matrix. The magnified SEM image clearly reveals a well-defined monolithic stack consisting of the OLED, TFE, QD/PDL, and DBR layers.

To further investigate the morphological characteristics of the patterned DBR stack on the integrated sub-pixel array, top-view and tilted-view SEM analyses were performed (Fig. S9). As shown in the top-view SEM images (Fig. S9a and c), our optimized dry-etching recipe maintains good pattern fidelity and edge definition across the sub-pixel array. On a flat control substrate (Fig. 4), the uniform photoresist thickness and flat underlying topography enable directional, highly anisotropic ion bombardment, yielding a near-vertical DBR sidewall profile. In contrast, for the fully integrated panel, when the QD photoresist is filled within the pixel-defining layer (PDL) matrix, capillary forces and solvent evaporation inherently cause the QD film to adopt a slightly concave surface profile (Fig. S9b). Additionally, a minor step height exists between the PDL bank and the filled QD layer, resulting in a complex non-planar topography across the pixel boundaries. As a result, the taper angle on the integrated device can be less vertical than that achieved on a flat test substrate. Nevertheless, as evidenced by the top-view and tilted-view SEM analyses (Fig. S9a–d), despite these challenging topographical variations, the DBR stack is fairly well patterned with distinct boundary definition and uniform pixel isolation across the array.

In terms of optical characteristics at the sub-pixel boundaries, the slanted sidewall profile reduces the effective top footprint of the DBR stack relative to the underlying QD sub-pixel. Consequently, the DBR cannot fully cover the entire top surface of the QD pixel, leaving exposed edge regions where blue photons escape without being reflected. As display resolution increases and sub-pixel dimensions shrink, the perimeter-to-area ratio inherently increases, exacerbating this localized edge leakage effect. At our current sub-pixel dimension (60 μm), this localized edge leakage remains minor and does not induce severe inter-pixel color crosstalk. However, as

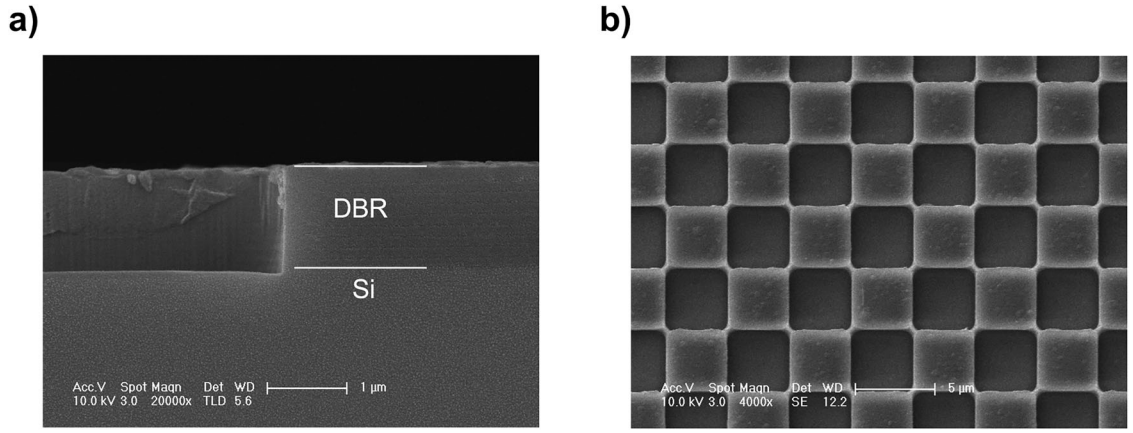


Fig. 4 | Scanning electron microscopy (SEM) images of the patterned DBR. **a** Cross-sectional SEM image of the dry-etched SiO_x/SiN_x DBR stack on a silicon substrate, showing a nearly vertical sidewall profile. Scale bar, 1 μm. **b** Top-view SEM image of the patterned DBR array with a pattern size of approximately 4 μm, corresponding to a pixel density of 3175 pixels per inch (ppi). Scale bar, 5 μm.

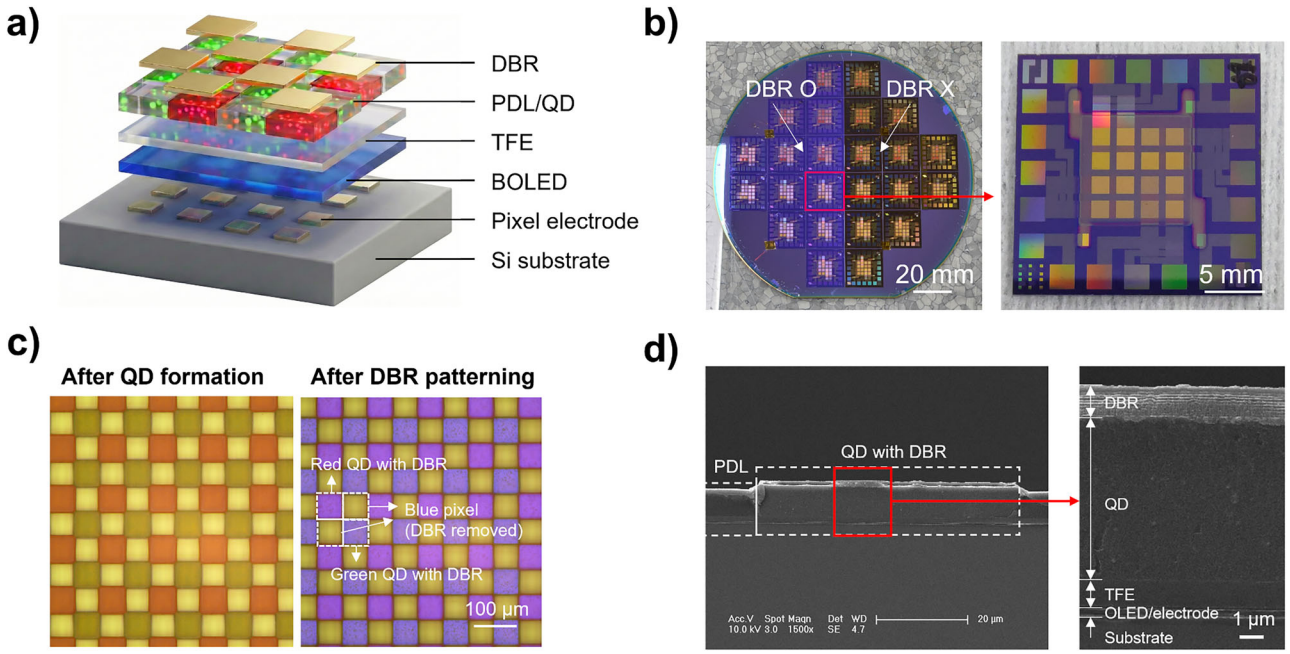


Fig. 5 | Monolithic integration of the QD-OLED with a patterned DBR. **a** Schematic illustration of the monolithically integrated top-emission QD-OLED structure with a selectively patterned DBR layer, depicting the layer stack consisting of a silicon substrate, top-emission blue OLED, TFE protection layer, QD color-conversion layers confined within PDL wells, and selectively patterned DBR residing over red and green sub-pixels. **b** Photographs of the fabricated device on a 6-inch wafer scale, showing regions with (DBR O) and without (DBR X) the DBR (left), and a magnified image of a single 20 mm × 20 mm device chip (right). Scale bars, 20 mm (left) and 5 mm (right). **c** Optical microscopy images of the pixel arrays after QD formation (left) and subsequent selective DBR patterning (right), showing a 60 μm sub-pixel size with the DBR aligned over red and green pixels and removed from blue pixel regions. Scale bar, 100 μm. **d** Cross-sectional SEM images of the monolithically integrated QD-OLED, showing the overall layer profile confined within the pixel defining layer matrix (left; scale bar, 20 μm) and a magnified view of the integrated stack consisting of the substrate, OLED/electrode, TFE, QD layer, and DBR stack (right; scale bar, 1 μm). The author designed Fig. 5a in Microsoft PowerPoint and used Google Gemini only to improve its visual quality. No third-party copyrighted materials, external sources, or stock images were used or adapted.

pixel dimensions shrink further, this localized edge leakage could become a potential limitation for optical purity. Therefore, our findings suggest that eliminating surface non-planarity to achieve ideal vertical coverage becomes increasingly essential for ultra-high-resolution display applications, which could be effectively addressed through an additional planarization step.

As observed in the SEM analyses (Fig. S9), the QD-PR layer exhibits noticeable surface roughness and non-planar topography. To quantitatively verify the surface quality, atomic force microscopy (AFM) analysis of the QD-PR films was performed (Fig. S10). The red and green QD-PR films exhibited root-mean-square roughness (R_q) values of 1.70 nm and 2.46 nm, and peak-to-valley roughness (R_{pv}) values of 23.3 nm and 22.0 nm, respectively. Although the overall R_q remains relatively low, the localized peak-to-valley roughness (~ 23 nm) indicates the presence of nanoscale topographical variations and isolated nano-aggregates within the matrix. Because the multilayer DBR stack was deposited directly onto the patterned QD-PR layer without a separate planarization step, this underlying surface roughness conformally propagates into the overlying SiO_x/SiN_x dielectric interfaces. While the DBR stack maintains physical structural integrity, the propagated interfacial roughness and isolated nano-aggregates can induce

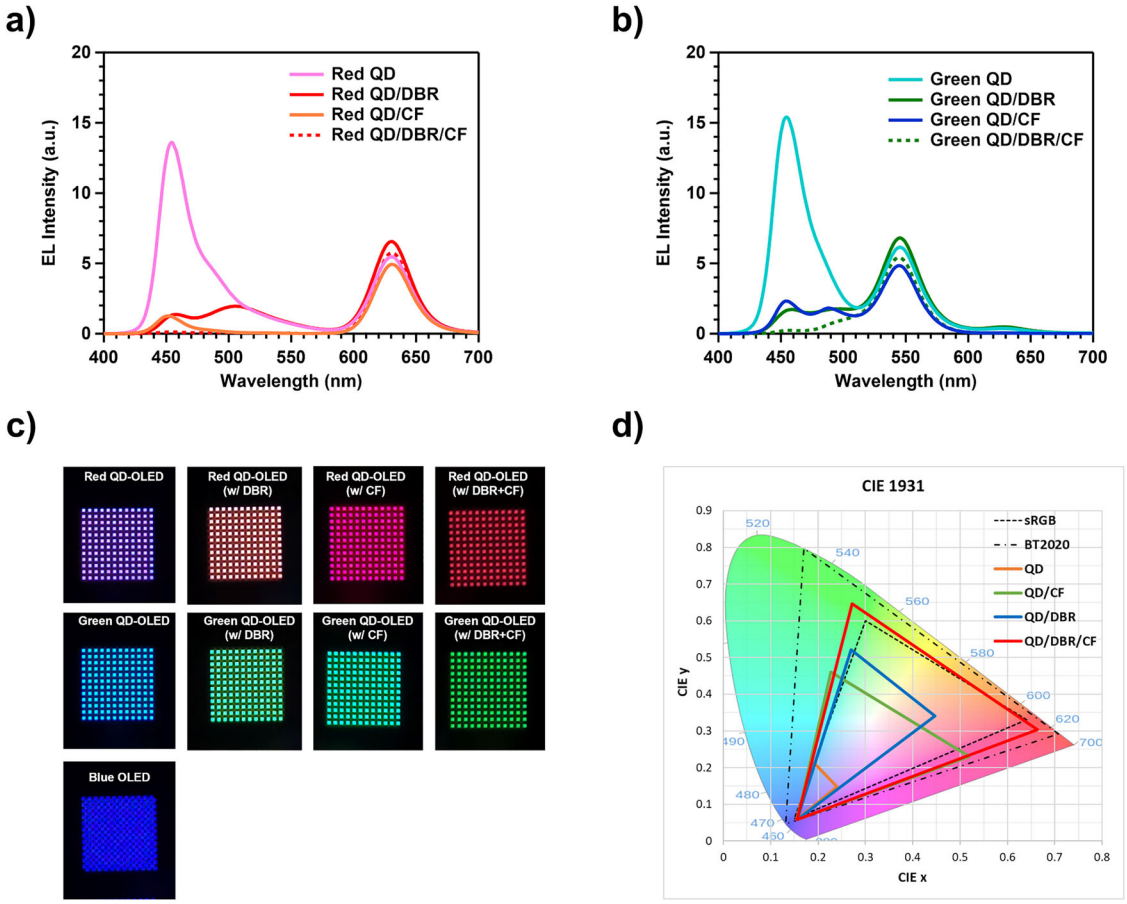


Fig. 6 | Electroluminescence (EL) spectra, emission photographs, and color gamut characteristics across different optical configurations. a EL spectra of red QD-OLEDs comparing four configurations: bare red QD (pink solid line), red QD/DBR (red solid line), red QD/CF (orange solid line), and red QD/DBR/CF (red dashed line). The DBR integration suppresses blue light leakage while enhancing red QD emission via photon recycling, and the combined DBR/CF structure eliminates residual blue leakage. **b** EL spectra of green QD-OLEDs comparing four configurations: bare green QD (cyan solid line), green QD/DBR (olive green solid line), green QD/CF (blue solid line), and green QD/DBR/CF (green dashed line). Similarly, the DBR reduces blue leakage and increases green emission, whereas the dual DBR/CF filter effectively suppresses blue light leakage. **c** Electroluminescence photographs of operating red and green QD-OLED pixel arrays for each optical configuration, showing that applying either DBR or CF improves color purity, whereas the combined QD/DBR/CF architecture considerably enhances color purity toward primary red and green emissions. **d** Commission Internationale de l'Éclairage (CIE) 1931 chromaticity diagram comparing color gamuts for QD (orange line), QD/CF (green line), QD/DBR (blue line), and QD/DBR/CF (red line) against standard sRGB (black dashed line) and Rec. 2020 (BT.2020, black dash-dotted line) boundaries, demonstrating that single-component integration (DBR or CF) expands the color gamut, while the combined QD/DBR/CF configuration achieves a significant gamut expansion.

localized changes in interference conditions and light scattering, contributing to increased blue light leakage.

The electroluminescence of the monolithically integrated QD-OLED was evaluated to quantify the individual and combined effects of the patterned DBR and CF (transmittance shown in Fig. S11) on color purity and efficiency. Figure 6a, b presents the EL spectra for the red and green pixels, respectively, under four different configurations: QD only, QD/DBR, QD/CF, and QD/DBR/CF. For the red pixels, the integration of the DBR (Red QD/DBR) resulted in a significant reduction in blue leakage at 455 nm, decreasing the intensity from 1.36×10^{-2} to 1.22×10^{-3} (~ 91% reduction). Simultaneously, the primary red emission at 630 nm increased from 5.47×10^{-3} to 6.55×10^{-3}, representing a 19.7% enhancement in emission intensity attributable to the photon recycling effect. In contrast, QD with the CF only (Red QD/CF) suppressed blue leakage through absorption but yielded a lower red peak intensity compared to the DBR-integrated pixel due to the absence of photon recycling. When the CF was added to the QD/DBR structure (Red QD/DBR/CF), the blue leakage was further suppressed to a negligible level of 0.0001. A similar trend was observed for the green pixels. The blue leakage at 455 nm dropped from 1.54×10^{-2} to 1.67×10^{-3} after DBR integration (~ 89% reduction), while the green emission peak at 546 nm exhibited a clear enhancement from 6.14×10^{-3} to 6.80×10^{-3} (10.7% increase). The CF-only configuration (Green QD/CF) suppressed blue leakage through absorption but exhibited lower peak intensity. These results provide direct experimental evidence that the patterned DBR effectively reflects the non-absorbed blue light back into the QD layer, where it is re-absorbed and converted into primary color photons.

To further examine the electrical and overall optical performance of the device, the current density–voltage–luminance (J–V–L) characteristics and current efficiency (CE) curves for each configuration are provided in Fig. S12. As shown in Fig. S12, the J–V behaviors are consistent across all configurations, confirming that monolithic integration does not degrade the electrical properties of the underlying blue OLED. In contrast, the luminance varies depending on the emission wavelength and optical stack configuration due to spectral conversion and filtering effects. Furthermore, the CE decreases upon CF integration, because the CF suppresses the dominant blue leakage while partially absorbing the target QD emission. In addition, the QD/DBR/CF structure exhibits a slightly higher total CE than the QD/CF configuration despite lower blue leakage, confirming that the patterned DBR enhances QD emission through photon recycling.

While the standalone DBR stack evaluated in an ex-situ setup exhibited a high reflectance of 95.9% at 455 nm, the blue light reduction in the monolithically integrated device was measured at approximately 90%, which is lower than the theoretical expectation. This performance difference can be attributed to the structural transition from an ex-situ stacked setup to monolithic direct deposition on a micro-patterned film. To further investigate this discrepancy and the spatial distribution of the residual blue leakage, 2D spectroradiometric analysis was performed as shown in Figure. S13. The intensity mappings at 455 nm (Fig. S13b and e) demonstrate that the leakage is not spatially uniform; rather, it is concentrated at the pixel boundaries and in proximity to scattering agents within the QD matrix. Point-wise spectral analysis in Figure. S13c and f provides a detailed comparison of the emission characteristics across different pixel regions. Point 1 identifies a bright spot within the pixel center where blue leakage is locally high, which may be attributed to propagated interfacial roughness and localized light scattering potentially stemming from embedded scattering particles and surface non-uniformities as observed in Figs. S9 and S10. In contrast, point 2 represents a normal region where the blue light is effectively suppressed by the DBR. Unlike the ex-situ setup where an air interface decouples the DBR from the QD matrix, direct deposition in the integrated panel allows photons scattered by internal scattering particles or localized surface roughness to propagate directly into the overlying dielectric multilayers without an air-gap buffer. Blue leakage is also observed at the pixel edges (Point 3). As shown in Fig. S9, the QD pattern was formed slightly larger than the overlying DBR stack at the sub-pixel boundaries, leaving the peripheral edges of the QD layer partially uncovered by the DBR. As a result, a small fraction of blue light bypassed the dielectric filter and leaked directly through these exposed QD margins. Collectively, these patterning-induced edge leakage effects and direct-contact interfacial roughness and scattering dynamics can account for the slight degradation in blue light filtering performance observed in the macroscopic spectra.

Figure 6c shows the emission photographs of the red and green QD-OLEDs across four distinct optical configurations. Without the DBR or CF, the red and green pixels appear purple and sky-blue, respectively, indicating that blue light leakage significantly reduced color purity. The introduction of either a DBR or CF improves color purity, whereas the combined QD/DBR/CF structure approaches primary red and green colors more closely than either DBR or CF alone. Notably, subtle differences in color are observed between the single-component configurations (QD/DBR vs. QD/CF). For the red pixels, the QD/CF structure exhibits a more reddish hue than the QD/DBR structure. This is attributed to the absorption profile of the red CF, which more effectively eliminates the blue emission shoulder near 500 nm, whereas the DBR exhibits partial transmission near its long-wavelength cutoff edge. Conversely, for the green pixels, the QD/DBR structure exhibits a more greenish hue than the QD/CF structure. While both the green CF and DBR exhibit similar suppression near 500 nm, the QD/CF structure suffers from a lower green QD peak intensity due to the absence of photon recycling, resulting in a reduced green purity relative to QD/DBR.

Figure 6d illustrates the Commission Internationale de l'Éclairage (CIE) 1931 color coordinates across the four optical configurations, with the corresponding relative color gamut summarized in Table 2. Due to the substantial blue leakage, the bare QD-OLED achieves an extremely low color gamut of 4.8% relative to standard red, green, blue (sRGB) color space (2.5% for Rec. 2020). Integrating the CF alone improves the color gamut to 59.9% of sRGB (31.7% for Rec. 2020), whereas implementing the patterned DBR alone expands the gamut to 45.9% of sRGB (24.3% for Rec. 2020), and combining both the DBR and CF achieves a color gamut of 120.5% of sRGB (63.7% for Rec. 2020).

Table 2 | Comparison of relative color gamut (sRGB and Rec. 2020 standards) for QD-OLED devices across four different optical configurations

Optical Configuration	sRGB (%)	Rec. 2020 (%)
QD-OLED (without DBR and CF)	4.8	2.5
QD-OLED with CF only (without DBR)	59.9	31.7
QD-OLED with DBR only (without CF)	45.9	24.3
QD-OLED with both DBR and CF	120.5	63.7

Toward the Rec. 2020 standard, the color gamut achieved in this study is still insufficient. This is primarily due to the long-wavelength emission tail of the blue OLED source near 500 nm and the low absorption coefficient of the eco-friendly InP-based QDs within the thin photoresist layer. However, the architecture developed in this study establishes a highly promising framework that enhances conversion efficiency through photon recycling within a limited film thickness. As high-absorbance eco-friendly QDs and blue OLEDs with narrower full-width at half-maximum (FWHM) continue to advance, this platform will offer a viable pathway to approach the Rec. 2020 standard even at a thickness of only a few microns. Therefore, this work provides a highly effective and versatile strategy for realizing high-performance QD-OLED microdisplays with superior color purity and efficiency.

Discussion

In this study, we successfully demonstrated the monolithic integration of DBRs into QD-OLEDs to achieve superior color purity and enhanced efficiency. The DBR, composed of SiN_x and SiO_x layers and fabricated using a low-temperature PECVD process, was optimized to provide a high reflectance of 95.9% at the target blue wavelength (455 nm) while effectively suppressing reflection in the red and green regions. The development of a high-precision, one-step fluorine-based dry-etching process enabled the formation of fine DBR patterns with a feature size of 4 μm and a near-vertical taper angle of 89°, supporting pixel densities up to 3175 ppi. By monolithically integrating these robust, high-resolution DBRs into the QD-OLED architecture, we achieved QD emission enhancements of 19.7% for red pixels and 10.7% for green pixels, while simultaneously reducing blue light leakage by approximately 90%. With the addition of a color filter (CF), the integrated device achieved a color gamut of 120.5% relative to the sRGB standard. These findings confirm that monolithically integrated, low-temperature-processed DBRs offer a robust and scalable solution for the next generation of high-performance displays, providing both high resolution and improved color quality in QD-OLED technology.

Nevertheless, several technical challenges must be addressed to realize full ultra-high ppi active microdisplays for AR/VR applications. The low optical absorbance of current eco-friendly QDs requires relatively thick QD-PR layers, yielding high aspect ratios that hinder high-resolution patterning. Although internal scattering particles enhance absorption, they cause UV scattering during photolithography—compromising patterning fidelity and increasing surface roughness—which dictates the need for high-absorbance QDs that eliminate scattering agents. Furthermore, shrinking pixel pitch exacerbates lateral blue leakage and optical crosstalk. While a black matrix can mitigate sidewall leakage, high aspect ratio structures suffer from severe light loss; simultaneously, scattering particles induce backscattering at the TFE/QD interface into adjacent sub-pixels. Finally, high-precision multilayer DBR patterning requires strict surface planarization, which is hindered by QD surface roughness and step heights from PDLs. Despite these technical integration challenges, our study validates the direct integration of DBR stacks and identifies key process bottlenecks. Coupled with ongoing advances in QD materials and structural designs, these findings serve as a vital stepping stone toward future ultra-high-ppi QD-OLED microdisplays.

Methods

DBR simulation, fabrication, and characterization

The reflectance of the DBR structures was evaluated using the transfer matrix method under normal-incidence conditions. For each layer j, the optical characteristics were described by its complex refractive index, $\tilde{n} = n - ik$, and the corresponding characteristic matrix. The total transfer matrix of the multilayer stack was obtained by sequential multiplication of the characteristic matrices of all layers, calculating the effective input

admittance and reflectance. Furthermore, admittance trajectory diagrams were constructed in the complex admittance plane, tracing the evolution of the effective admittance through the stack. The refractive indices and extinction coefficients were measured using a spectroscopic ellipsometer (M-2000D; J. A. Woollam). The DBR was fabricated via low-temperature-processed PECVD at 100 °C. The reflectance of DBR was measured using the UV/Vis/NIR spectrophotometer (Lambda 1050, Perkin Elmer) based on the Universal Reflectance Accessory with an incidence angle of 8°. Cross-sectional images of the DBR were obtained using a precision ion-polishing system (PIPS 691; Gatan) and a transmission electron microscope (JEM-2100F; JEOL).

QD-OLED fabrication and characterization

Initially, ITO (5 nm)/Ag (100 nm)/ITO (5 nm) electrodes patterned on a 20 mm × 20 mm glass substrate were sequentially cleaned with acetone, isopropyl alcohol, and deionized water for 15 min. The substrates were then dried in a vacuum oven at 80 °C. Subsequently, 1,4,5,8,9,11-hexaazatriphenylene-hexacarbanitrile (HAT-CN; 10 nm), hole transport layer (150 nm), emission layer (EML; 20 nm), electron transport layer (40 nm), Mg:LiF(1:1; 1 nm), Mg:Ag(1:9; 15 nm), capping layer (80 nm), and LiF (50 nm) were thermally deposited to fabricate the blue OLED. The EML was co-deposited on the host material with the 6% fluorescent blue dopant. Detailed information on the OLED materials and design has been described in previous studies[37–39]. To passivate the OLED, 60-nm-thick Al_2O_3 was deposited via atomic layer deposition at 100 °C. The QD-OLED was fabricated by spin-coating red and green QD photoresist (QD-PR) onto the OLED at 500 rpm for 30 s, resulting in a QD layer thickness of 7–8 μm. The QD-PR solution was supplied by Dongjin Semichem Co., Ltd. These mixtures consisted of 30 wt% InP/ZnSe/ZnS core-shell QDs, monomers, binders, photo-initiators, and TiO_2 scattering agents. To ensure uniform dispersion within the PR resin matrix, the oleic acid/oleylamine ligands on the QD surfaces were substituted with thiol-functionalized moieties through a ligand exchange process. The absorbance and photoluminescence (PL) spectra of the red and green QD-PRs with different thicknesses are presented in Fig. S14. After spin-coating, the QD-OLED samples were soft-baked on a hotplate at 90 °C for 100 s and then exposed to UV light with a dose of 250 mJ/cm² under a nitrogen atmosphere. Finally, the QD-OLED was hard-baked in an oven at 85 °C for 1 h.

The color conversion characteristics were evaluated by measuring the *J–V–L* characteristics of QD-OLEDs in a dark room using a source measurement unit (Keithley 238) and a spectroradiometer (CS-2000; Konica Minolta). The DBR was fabricated on each substrate and measured based on their contact with the QD-OLEDs. The red and green CFs (Dongjin Semichem Co., Ltd.) were prepared by spin-coating the CFs onto glass substrates at a speed of 2000 rpm for 30 s. The samples were soft-baked on a hotplate at 90 °C for 100 s and exposed to UV light at a dose of 100 mJ/cm² in a nitrogen atmosphere. Finally, the samples were hard-baked in an oven at 100 °C for 1 h. 2D EL mapping images and point spectra of monolithically integrated QD-OLEDs with patterned DBR were obtained using a 2D spectroradiometer (SR-5000; TOPCON) combined with an optical microscope (ECLIPSE LV100ND; Nikon).

To prepare samples for operational photostability testing, QD-PR were spin-coated onto glass substrates at 300 rpm for 30 s and subsequently baked at 100 °C for 1 h. The resulting QD thin films were encapsulated inside an N_2-filled glovebox using cavity glass covers. A getter was placed inside the cavity, and a UV-curable resin was applied along the edges of the cavity glass, followed by UV curing to ensure hermetic sealing (Glass/QD/Glass structure). The operational photostability of the encapsulated QD films was evaluated under continuous irradiation from a 450 nm blue LED source (SLSNNBA825TS) at an intensity of 70 W/m² for 1,000 h. During the test, emission spectra were recorded using a spectroradiometer (CS-2000, Konica Minolta), and the relative ratio of the QD PL peak intensity to the blue excitation peak intensity was monitored to determine the degradation over time.

DBR patterning process

A dry-etching process was employed to achieve high-resolution DBR patterning. Initially, hexamethyldisilazane (HMDS) was spin-coated onto the DBR substrate to enhance PR adhesion. A positive-tone PR was then spin-coated to obtain a sample with a thickness of approximately 3 μm. Subsequently, the PR was soft-baked at 90 °C for 60 s. The PR-coated substrates were selectively exposed to UV light at a dose of 350 mJ/cm² using an i-line stepper (NSR2205i11D; Nikon). After exposure, the PR was subjected to a post-exposure bake at 110 °C for 90 s and was developed using a puddling process with 2.38% tetramethylammonium hydroxide solution. The HMDS coating, PR coating, soft baking, post-exposure baking, and development were performed using a track system (Mark-Vz Coater; TEL). The DBR patterning was followed by dry etching, performed using a dry etcher (P5000 MxP; AMAT) under the following conditions: a base pressure of 70 mTorr, radio frequency power of 500 W, an Ar gas flow rate of 90 sccm, a CF_4 gas flow rate of 50 sccm, and a total etching time of 380 s. The total etching time was divided into two sessions of 190 s each to prevent PR burning. After etching, the PR was removed using sequential plasma and wet-strip processes.

Fabrication of fully integrated QD-OLED with patterned DBR

The device was fabricated on a silicon substrate initially deposited with a 300-nm-thick SiO_2 insulation layer via PECVD. For the wiring lines, a 55-nm-thick Mo layer was deposited by DC sputtering and subsequently patterned. An 80-nm-thick SiO_2 interlayer was then deposited via PECVD, followed by via-hole etching to establish electrical connectivity. The pixel electrodes were formed by sputtering another 55-nm-thick Mo layer, which was then patterned and etched to define the pixel area. Next, a top-emission blue OLED was deposited by thermal evaporation, where the structure was the same as in the QD-OLED fabrication section. Following that, a hybrid TFE was applied to protect the OLED from successive photolithography processes. A 60-nm-thick Al_2O_3 layer was deposited using ALD, and was then followed by a 1-μm-thick SiN_x layer deposited via PECVD at 100 °C. After the TFE process, a dry etching process was performed to open the contact pads. The PDL and QD layers were sequentially patterned via photolithography. The substrate was treated with HMDS, followed by spin-coating a transparent negative-tone PR at 600 rpm for 30 s. After soft-baking at 85 °C for 120 s, the layer was exposed using an i-line stepper (100 mJ/cm²), developed in a 2.38% TMAH solution for 150 s, and hard-baked at 100 °C for 2 h. For the green QD layer, the QD PR was coated at 1000 rpm for 30 s, soft-baked at 90 °C for 100 s, and exposed at 150 mJ/cm². Development was performed using a 0.04% KOH spray for 240 s, followed by hard-baking at 100 °C for 1 h. The red QD layer was coated at 2000 rpm for 30 s, soft-baked at 90 °C for 100 s, and exposed at 100 mJ/cm². It was developed with 0.04% KOH spray for 180 s and hard-baked at 100 °C for 1 h. After PDL/QD formation, a 30-nm-thick Al_2O_3 buffer layer was deposited via ALD to provide QD protection and serve as an etch-stop layer for the subsequent DBR patterning. After forming the 20-layer DBR stack, a 3-μm-thick PR mask was patterned. The DBR was then selectively removed from the blue pixel regions using the aforementioned dry etching conditions for a total of 380 s. Finally, the PR mask was stripped to complete the monolithic integration.

Use of artificial intelligence (AI)

During the preparation of this manuscript, the authors used Google Gemini to assist in refining the schematic illustration in Fig. 5a. All AI-assisted outputs were carefully reviewed, verified, and edited by the authors. The authors take full responsibility for the final content, integrity, and scholarly evaluation presented in this publication, in compliance with Springer Nature AI policy.

Data availability

The datasets generated and/or analyzed during the current study are not publicly available because the datasets are still being used for subsequent

related research, but are available from the corresponding author on reasonable request.

Received: 8 June 2026; Accepted: 1 October 2026;
Published online: 15 October 2026

References

1. Cho, H. et al. Exploration of OLED structures for high-resolution microdisplays with enhanced efficiency and color gamut. *J. Inf. Disp.* **25**, 261–269 (2024).
2. Wen, Z. et al. Color revolution: Toward ultra-wide color gamut displays. *J. Phys. D: Appl. Phys.* **54**, 213002 (2021).
3. Cho, H. et al. Organic light-emitting diode structure for high color gamut in high-resolution microdisplay: Over 90% color gamut based on BT.2020. *Org. Electron.* **101**, 106419 (2022).
4. Kim, J., Roh, J., Park, M. & Lee, C. Recent advances and challenges of colloidal quantum dot light-emitting diodes for display applications. *Adv. Mater.* **36**, 2212220 (2024).
5. Hahm, D. et al. Direct patterning of colloidal quantum dots with adaptable dual-ligand surface. *Nat. Nanotechnol.* **17**, 952–958 (2022).
6. Shu, Y. et al. Quantum dots for display applications. *Angew. Chem. Int. Ed.* **132**, 22496–22507 (2020).
7. Zheng, X. et al. V-pit-induced electric field redistribution enabling efficient hole injection in InGaN-based red light-emitting diodes grown on silicon. *PhotoniX* **6**, 55 (2025).
8. Wang, T. Prospect of developing III-nitride microLED technologies for micro-displays, visible light communications and artificial intelligence. *Prog. Quantum Electron.* **108**, 100634 (2026).
9. Jang, E. et al. White-light-emitting diodes with quantum dot color converters for display backlights. *Adv. Mater.* **22**, 2979–3092 (2010).
10. Hu, Z. et al. Inkjet printed uniform quantum dots as color conversion layers for full-color OLED displays. *Nanoscale* **12**, 2103–2110 (2020).
11. Plante, I. J.-L. et al. Quantum dot color conversion for displays. *SID Symp. Dig. Tech. Pap.* **54**, 792–794 (2023).
12. Tangirala, R. et al. Quantum dot color conversion for OLED and microLED displays. *SID Symp. Dig. Tech. Pap.* **52**, 906–908 (2021).
13. Palomaki, P. & Twietmeyer, K. Optical modeling of quantum dot-OLED (QD-OLED) color conversion. *SID Symp. Dig. Tech. Pap.* **53**, 303–306 (2022).
14. Xuan, T., Shi, S., Wang, L., Kuo, H.-C. & Xie, R.-J. Inkjet-printed quantum dot color conversion films for high-resolution and full-color micro light-emitting diode displays. *J. Phys. Chem. Lett.* **11**, 5184–5191 (2020).
15. Wang, X., Bao, Z., Chang, Y.-C. & Liu, R.-S. Perovskite quantum dots for application in high color gamut backlighting display of light-emitting diodes. *ACS Energy Lett.* **5**, 3374–3396 (2020).
16. Park, H. et al. Efficient quantum dot color conversion layer with mixed spherical/rod-shaped scattering particles. *ACS Appl. Opt. Mater.* **1**, 289–297 (2023).
17. Kim, Y.-J., Kim, H.-J., Um, K., Yang, H. & Lee, K. Application of quantum-dot patterned film with scattering nanoparticles for the high efficiency displays. *SID Symp. Dig. Tech. Pap.* **50**, 572–574 (2019).
18. Hyun, B.-R. et al. Dual role of quantum dots as color conversion layer and suppression of input light for full-color micro-LED display. *J. Phys. Chem. Lett.* **12**, 6946–6954 (2021).
19. Weng, Y. et al. Fabrication and color conversion of patterned InP/ZnS quantum dots photoresist film via a laser-assisted route. *Opt. Laser Technol.* **140**, 107026 (2021).
20. Chu, S.-Y. et al. Improved color purity of monolithic full color micro-LEDs using distributed Bragg reflector and blue light absorption material. *Coatings* **10**, 436 (2020).
21. Weng, Y. et al. Design and fabrication of bi-functional TiO_2/Al_2O_3 nanolaminates with selected light extraction and reliable moisture vapor barrier performance. *Nanotechnology* **30**, 085702 (2019).
22. Lee, T.-Y. et al. Ameliorating uniformity and color conversion efficiency in quantum dot-based micro-LED displays through blue–UV hybrid structures. *Nanomaterials* **13**, 2099 (2023).
23. Gao, Y. et al. Research on etching of distributed Bragg reflector. *J. Phys. Conf. Ser.* **2645**, 012005 (2023).
24. Yu, W. et al. Semitransparent polymer solar cells with 5% power conversion efficiency using photonic crystal reflector. *ACS Appl. Mater. Interfaces* **6**, 599–605 (2014).
25. Zhang, D.-D. et al. Enhanced performance of semitransparent inverted organic photovoltaic devices via a high reflector structure. *ACS Appl. Mater. Interfaces* **5**, 10185–10190 (2013).
26. Dang, G. et al. Comparison of dry and wet etch processes for patterning SiO_2/TiO_2 distributed Bragg reflectors for vertical-cavity surface-emitting lasers. *J. Electrochem. Soc.* **148**, G25–G28 (2001).
27. Setyawati, O. et al. Characterization of dry etching of TiO_2/SiO_2 distributed Bragg reflectors for tunable optical sensor arrays. *J. Micro/Nanolith. MEMS MOEMS* **9**, 041110 (2010).
28. Taimoor, M., Alatawi, A., Reuter, S., Hillmer, H. & Kusserow, T. Single-step inductively coupled plasma etching of sputtered Nb_2O_5/SiO_2 multilayer stacks using chromium etch mask. *J. Vac. Sci. Technol. A* **35**, 041302 (2017).
29. Xu, J. et al. Design and optimization of red-light reflector using simulation software. *Sens. Mater.* **33**, 2619–2627 (2021).
30. Lin, K.-C. et al. Modified distributed Bragg reflector for protecting organic light-emitting diode displays against ultraviolet light. *Opt. Exp.* **29**, 7654–7665 (2021).
31. Shin, Y. et al. Environmentally stable luminescent perovskite nanocrystals passivated and encapsulated by siloxane hybrids enabling reliable color-converted organic light-emitting diodes. *Chem. Eng. J.* **474**, 145889 (2023).
32. Lv, X. et al. Extending the π-skeleton of multi-resonance TADF materials towards high-efficiency narrowband deep-blue emission. *Angew. Chem. Int. Ed.* **61**, e202201588 (2022).
33. Cheng, C. et al. Extremely stable deep-blue organic light-emitting diodes employing diindolophenazine-based fluorophore with narrow-band emission and a shallow LUMO level. *Chem. Eng. J.* **474**, 145691 (2023).
34. Lee, S. H. et al. Enhanced triplet-triplet fusion for high efficiency and long lifetime of multiresonant pure blue organic light emitting diodes. *J. Ind. Eng. Chem.* **122**, 452–458 (2023).
35. Ye, J. et al. Dry etching characteristics of titanium dioxide grown by different physical vapor deposition processes. *J. Vac. Sci. Technol. B* **43**, 052203 (2025).
36. Park, M., Yoon, I. & Park, Y. Etching for vertical sidewall formation in TiO_2 nanorods. *Appl. Sci. Converg. Technol.* **31**, 113–115 (2022).
37. Cho, H. et al. Highly conductive and transparent thin metal layer for reducing microcavity effect in top-emitting white organic light-emitting diode. *Org. Electron.* **106**, 106537 (2022).
38. Lee, S. J. et al. Three-wavelength white organic light-emitting diodes on silicon for high luminance and color gamut microdisplays. *J. Ind. Eng. Chem.* **105**, 132–137 (2022).
39. Cho, H. et al. Correlation between optimized thicknesses of capping layer and thin metal electrode for efficient top-emitting blue organic light-emitting diodes. *ETRI J.* **45**, 1056–1064 (2023).

Acknowledgements

This study was partially supported by the Korea Evaluation Institute of Industrial Technology (KEIT) grant funded by the Ministry of Trade, Industry & Energy (MOTIE, Korea; No. 20015805, Development of material parts and processing technology for post-InP fluorescence quantum dots), the Institute of Information & Communications Technology Planning & Evaluation (IITP) grant funded by the Korean government (MSIT) (No. 2022-0-00026, Near-eye light field device technology development for hyper-realistic metaverse service), National Research Foundation of Korea (NRF) grants funded by the Ministry of Science and ICT (No. RS-2024-00445116) and the

Basic Science Research Program through the NRF funded by the Ministry of Education (No. 2018R1A6A1A03026005), and the Electronics and Telecommunications Research Institute (ETRI) grant funded by the Korean government (No. 26ZC1200, Research on Ultra-Realistic Spatial Device Technology). The funders played no role in study design, data collection, analysis, interpretation of data, or the writing of this manuscript.

Author contributions

J.-W.S., S.W.W., J.L. and C.-m.K. conceived the idea and designed the experiments. S.W.W. and J.Y.K. designed the structure of the DBR. S.W.W., H.J. and C.-m.K. measured and characterized the DBR. J.-W.S., S.W.W., H.C., S.C., B.-H.K. and C.-m.K. fabricated and characterized the QD-OLED. I.B. developed the fine patterning process of the DBR. H.M.Y., J.S.K., J.H.J., and J.Y.B. designed and fabricated the QD-PR. J.-W.S., H.C., S.C., G.H.K., B.-H.K. and C.-m.K. fabricated the monolithically integrated QD-OLED with patterned DBR. J.-W.S., H.J. and C.-m.K. measured the DBR-integrated QD-OLED characteristics. C.W.B. and N.S.C. analyzed the data. J.L. and C.-m.K. guided all aspects of the work. All authors discussed the results, contributed to the manuscript, and approved the final version.

Funding

The authors received no specific funding for this work.

Competing interests

The authors declare no competing interests.

Additional information

Supplementary information The online version contains supplementary material available at https://doi.org/10.1038/s41528-026-00652-3.

Correspondence and requests for materials should be addressed to Jonghee Lee or Chan-mo Kang.

Reprints and permissions information is available at http://www.nature.com/reprints

Publisher's note Springer Nature remains neutral with regard to jurisdictional claims in published maps and institutional affiliations.

Open Access This article is licensed under a Creative Commons Attribution-NonCommercial-NoDerivatives 4.0 International License, which permits any non-commercial use, sharing, distribution and reproduction in any medium or format, as long as you give appropriate credit to the original author(s) and the source, provide a link to the Creative Commons licence, and indicate if you modified the licensed material. You do not have permission under this licence to share adapted material derived from this article or parts of it. The images or other third party material in this article are included in the article's Creative Commons licence, unless indicated otherwise in a credit line to the material. If material is not included in the article's Creative Commons licence and your intended use is not permitted by statutory regulation or exceeds the permitted use, you will need to obtain permission directly from the copyright holder. To view a copy of this licence, visit http://creativecommons.org/licenses/by-nc-nd/4.0/.

© The Author(s) 2026

This Article in Press is shared early to give you faster access to new research. It is citable and carries a permanent DOI. The final edited version will replace it automatically.